Sensors & Actuators: B. Chemical 408 (2024) 135548

Contents lists available at ScienceDirect

Sensors and Actuators: B. Chemical

journal homepage: www.elsevier.com/locate/snb

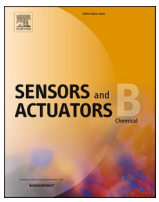

Insitu controllable synthesis of MoO_3 nanoflakes and its temperature-dependent dual selectivity for detection of ethanol and isopropanol

Wen Li [a], Hao Xu [a], Aiwu Wang [a], Xuelan Cheng [a], Jidong Shi [a], Aihua Zhong [b], Yujie Ma [a], Liaoyuan Zhang [a], Zhiyong Fan [c], Fang Xu [a,*]

[a] Shenzhen Key Laboratory of Ultraintense Laser and Advanced Material Technology, Center for Advanced Material Diagnostic Technology, and College of Engineering Physics, Shenzhen Technology University, Shenzhen 518118, China
[b] College of Physics and Optoelectronic Engineering, Shenzhen University, Shenzhen 518060, China
[c] Department of Electronic and Computer Engineering, The Hong Kong University of Science and Technology, Clear Water Bay, Kowloon, Hong Kong, China

ARTICLE INFO

Keywords:
MoO_3 nanoflakes
Ethanol
Isopropanol(IPA)
Gas sensor
Dual selectivity
Decreased critical temperatures

ABSTRACT

Nanostructures significantly affect the performance of metal oxide semiconductor (MOS) based gas sensors. Herein, we proposed a method of inducing sulfur-doping (S-doping) in the synthesis to control the morphology of MoO_3 nanoflakes. The MoO_3 nanoflakes prepared with increased S-doping have morphologies with decreased thickness, increased aspect ratio, increased surface area and increased surface chemisorbed oxygens, which improved sensing properties including higher response, better selectivity to ethanol and lower critical temperatures for the temperature-dependent dual selectivity. The response to 500 ppm ethanol at 350°C was improved by 3-fold as compared to the MoO_3 obtained without S-doping. The sensors exhibited a temperature-dependent dual selectivity to isopropanol (IPA) and ethanol. The critical temperatures exhibited a decreasing trend for the gas sensors made of MoO_3 which are obtained with increasing S-doping. The feasibility of inducing S-doping in the preparation to modify the morphology of MoO_3 nanoflakes and using it to enhance the gas sensing performance are reported for the first time. It should have a chance to be widely spread into the applications for which higher aspect ratio is beneficial, such as various sensors and photocatalysis.

1. Introduction

High-performance gas sensors play a vital role in daily life and production, such as monitoring toxic and hazardous gases [1,2], and in-vitro disease detection based on human exhaled gases [3–5], etc. Metal oxide semiconductor (MOS) based gas sensor is a promising class of solid-state gas sensors because of their high sensitivity, ease of fabrication, and low cost [6–8]. In 1962, it was demonstrated that the electrical conductivity of metal oxides can be altered by the adsorption and desorption of gas molecules on their surface [9], which is the fundamental idea behind conductive MOS based gas sensors. The sensing properties is heavily constrained by the morphology of the metal oxides [3,10–12]. The performance of a gas sensor is significantly impacted by the specific surface area and thickness of the material. A large surface area provides more active sites for gas molecules adsorption and sensing reactions, facilitating gas molecules diffusion into the oxide layer and resulting in rapid response kinetics for high response and better selectivity [14,16–18]. When the thickness of the semiconductor decreases to twice the Debye length, the depletion layer occupies the entire crystal. This indicates that the free carriers are effectively depleted [5]. At this point, the change in resistance of the material caused by the interaction between the gas and the material is transformed from a change in surface resistance to a more sufficient change in body resistance, resulting in a larger response [15,17]. Therefore, a significant amount of effort was dedicated to designing specially structured materials such as nanowires [18], nanocubes [3], and nanorices [19]. One-dimensional nanostructures are preferred for the applications of gas sensors due to their high specific surface area, larger surface-to-volume ratio, direct electron transporting path, and small thickness. Stacking one-dimensional structures will form a more loose sensing film which benefits the diffusion of the gas molecules [20].

As a typical n-type semiconductor oxide, MoO_3 is considered one of

* Correspondence to: Shenzhen Technology University, Room 612, 6/F, B4 Building, Pingshan, Shenzhen, Guangdong, China.
E-mail address: xufang@sztu.edu.cn (F. Xu).

https://doi.org/10.1016/j.snb.2024.135548
Received 17 October 2023; Received in revised form 31 January 2024; Accepted 24 February 2024
Available online 27 February 2024

the most promising semiconductor materials for various applications, including sensors [21–23], photocatalysts [24], solar cells [25], and thin film electrodes [26]. Various MoO_3 nanostructures have been reported for use in chemical sensors, such as ethanol [23], H_2S [27], NO_2 [28], H_2 [29]and methanol [30]. Nevertheless, there are rare reports on the study of morphology modulation of MoO_3 and its relevance with sensing performance.

Gas selectivity is a crucial performance metric in gas sensing. MOS based gas sensors often have a cross-response to various gases. The phenomenon that the response to the target gas is higher than that to the interfering gas is often referred to the gas selectivity [31,32]. Realizing selective detection of multiple gases using a single gas sensor is a focus of current research. Matteo Tonezzer et al. [33] have described the dual selectivity of gas sensors based on NiO polycrystalline nanowires for H_2 and ethanol. We have reported multifunctional gas sensors based on ZnO nanotetrapods for volatile organic compounds (VOCs) [31,34]. Ethanol and isopropanol (IPA) are two common VOCs used in production and daily life. Both of them have anesthetic or depressant effects on the central nervous system and prolonged exposure can cause severe cognitive impairment [18,35].

In this work, we reported a two-step method for preparing MoO_3 nanoflakes and using sulfur-doping (S-doping) to tune the morphology. Different morphologies of MoO_3 nanoflakes were obtained by varying the amount of S-doping in the solvothermal process, and their gas-sensitive properties were compared. Temperature-dependent dual selectivity and the critical temperatures were studied. The impropved sensing performance and the principle of temperature-dependent dual selectivity of MoO_3 nanoflakes were investigated based on the sensing mechanism.

2. Experimental section

2.1. Preparation of MoO_3 nanoflakes and gas sensor devices

The schematics for preparing MoO_3 nanoflakes is shown in Fig. 1. Commercial α-MoO_3 powder was used as the raw material whose morphology is shown in Fig. S1. 0.3 g α-MoO_3 powder was mixed with 0–0.6 g sulfur powder for various doping ratios of sulfur. The mixture was added into 20 mL N-methyl pyrrolidone (NMP)/H_2O mixed solvent with 1:1 vol ratio of NMP and H_2O. A homogeneous white suspension was obtained and stored for reaction in a vacuum drying oven at 120°C for 24 h. After that, it was centrifuged at 12000 rpm for 10 min and the supernatant was taken and stored in dark, followed by drying in a vacuum oven under vacuum at 120°C until obtaining black powder. This black powder was the sulfated MoO_{3-x} amorphous structure, defined as MoO_{3-x}/S. 0.25 mg MoO_{3-x}/S was mixed with 50 μL deionized water to form a black slurry. 3 μL of the black slurry was overcoated on the front side of a ceramic chip substrate, where a pair of Au electrodes were printed with a gap to establish contact between the sensing material and the ceramic substrate, each Au electrode connected with a Pt wire (Fig. S2(a)). An additional pair of Pt wires is connected to the back of the substrate to control its temperature. The ceramic substrate loaded with the black MoO_{3-x}/S film was welded into a six-pin base (Fig. S2(b)). This black device was then heated at 350°C for 2 h, and MoO_3 nanoflakes were obtained with the sensing surface of the device gradually turning from black to white as shown in Fig. S2(c). By now, the fabrication of gas sensors was completed. The sensors with 0 g, 0.15 g, 0.3 g and 0.6 g sulfur powder induced in the synthesis process were labeled as MO, MO-S(0.5), MO-S(1), and MO-S(2), respectively.

2.2. Characterizations

X-ray diffraction (XRD) patterns of the material were recorded on a SmartLab X-ray diffractometer (45 kV, 200 mA, Cu-Kα radiation, 10° ~ 80° min^{-1}). Field emission scanning electron microscopy (FESEM) images were acquired at 10 kV using a Carl Zeiss Microscopy Ltd. GeminiSEM 300 field emission scanning electron microscope (secondary electron resolution of 0.7 nm @15 kV, 1.2 nm @1 kV, accelerating voltage: 0.02 kV to 30 kV). Energy dispersive spectroscopy (EDS) analysis was accomplished from FESEM images using an Oxford Max100 EDS detector. X-ray photoelectron spectroscopy (XPS) analysis was performed on a Thermo Fisher Scientific (China) Co. Ltd XPS Escalab Xi^+ X-ray photoelectron spectrometer equipped with a Mg/Al double anode, UV photoelectron spectroscopy and a cluster ion gun (microfocused monochromatic Al Kα radiation with a calibration peak of C 1 s at 284.6 eV) was performed.

2.3. Gas sensing measurements

After the sensor devices undergoing an aging process at 150°C for 24 h, the gas sensing measurements were carried out on the gas sensing system WS-30B (Winsen Electronics Technology Co. Ltd., Zhengzhou, China). As shown in Fig. 2, the sensors were placed in the measurement chamber of WS-30B and the resistance of the sensors was recorded. A stationary gas distribution method was used to control the atmosphere in the chamber. The gas concentration is derived by formula of c =

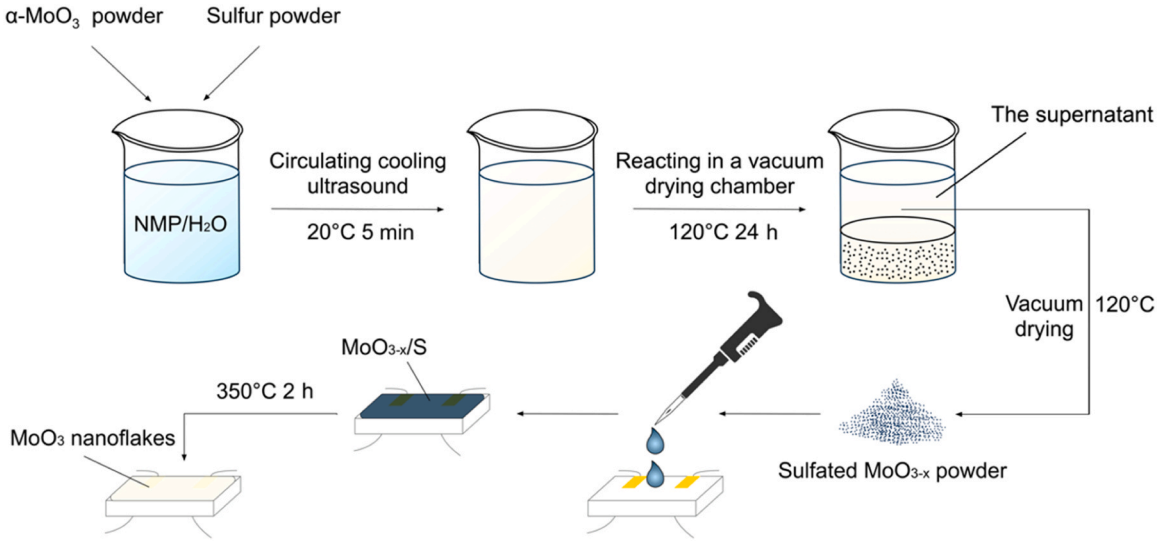

Fig. 1. Schematic illustration of the synthesis processes of MoO_3 nanoflakes.

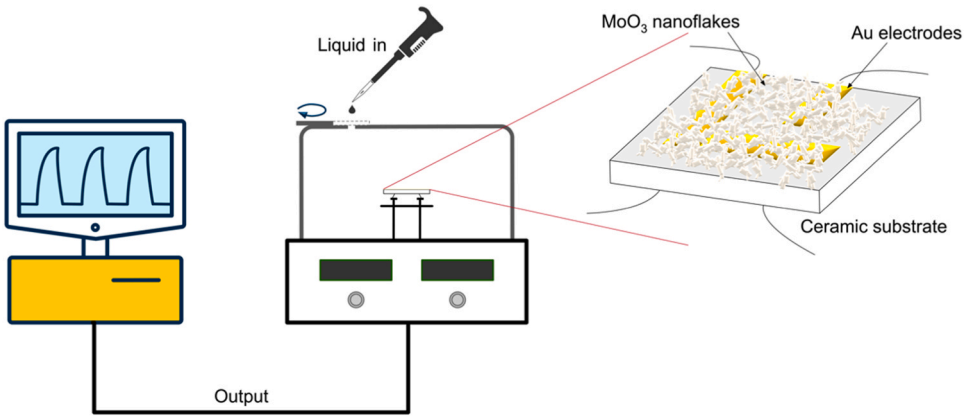

Fig. 2. Schematic diagram of the sensing measurements.

$\frac{22.4\times\rho\times d\times V_1}{M\times V_2}$, where V_2 is the volume of the measurement chamber, and V_1, M, ρ, and d are the volume, relative molecular mass, density, and purity of the liquid, respectively [10,20]. The sensing response is defined as R_a/R_g, where R_a and R_g represent the resistance of the device in air and in the target gas to be measured, respectively [20]. Response time (τ_{res}) is defined as the time required for the gas sensor to reach 90% of the stable resistance value from its contact with the gas to be measured. Recovery time (τ_{rec}) is defined as the the time required for a gas sensor to return to 90% of its stable resistance value in air after being re-exposed to clean air. The operating temperature of the sensors was measured with the infrared thermal imaging camera FOTRIC 340X (Parklane Technology Co. Ltd., Shenzhen, China).

3. Results and discussions

3.1. Materials characterizations

FESEM image of the raw material α-MoO_3, which exhibits a hierarchical structure, is shown in Fig. S1. As shown in Fig. 3(a) and Fig. S3, MO shows a porous hierarchical structure. As shown in Fig. 3(b-d), MO-S

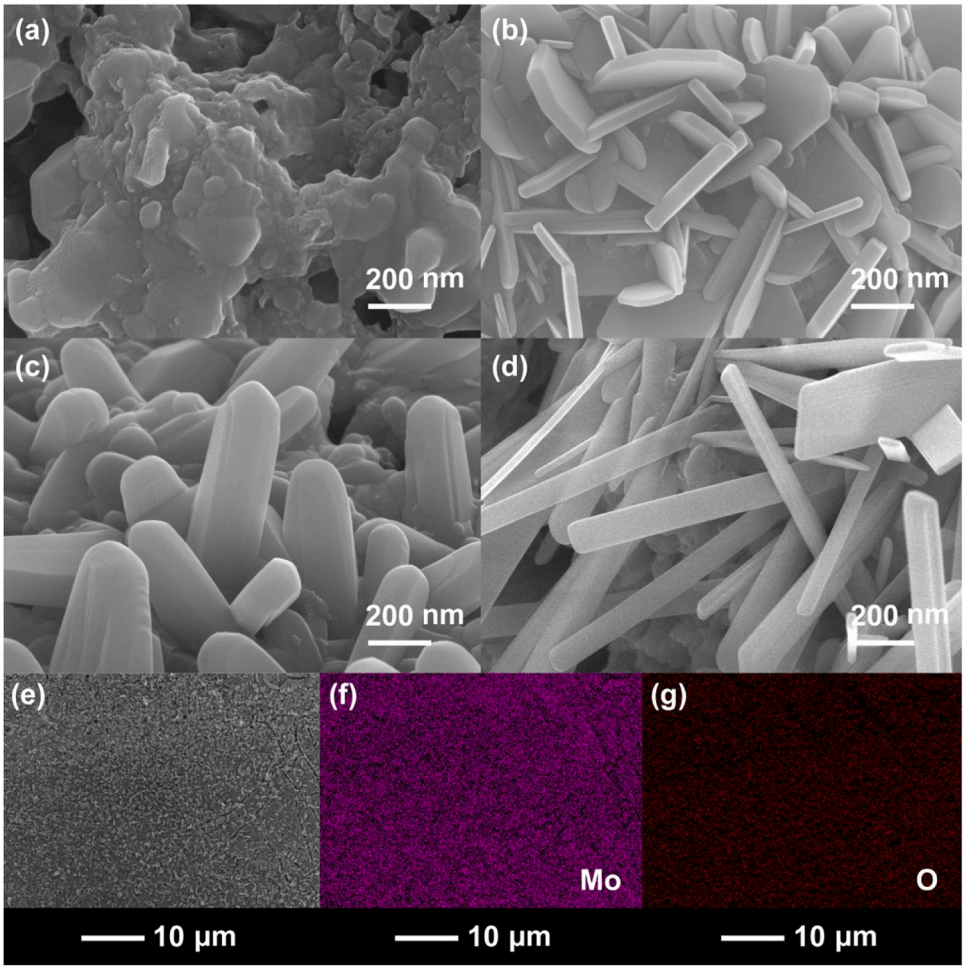

Fig. 3. FESEM images of (a)MO, (b)MO-S(0.5), (c)MO-S(1) and (d)MO-S(2). (e)-(g) EDS mapping images taken from FESEM image of MO-S(2).

(0.5), MO-S(1), and MO-S(2) show nanoflake structures respectively with an increased average aspect ratio of 1, 2, and 10, and an average thickness of 50, 80, 10 nm. The thickness is the smallest and the aspect ratio is the largest in MO-S(2). To investigate the specific growth process, we studied the FESEM of devices obtained by heating the black intermediate MoO_{3-x}/S samples at 350°C for 0 h, 0.5 h, and 1 h as shown in Fig. S4(a-c), respectively. The amorphous structure of the black intermediate MoO_{3-x}/S disappeared gradually and was replaced by an increasing amount of nanoflakes as the heating time increases. Furthermore, EDS patterns were used to investigate the elemental distribution. Mo, S and O elements are uniformly distributed in the EDS spectrum of the black intermediate MoO_{3-x}/S as shown in Fig. S4(d-g), suggesting successful S-doping in the black intermediate MoO_{3-x}/S. EDS patterns of white MO-S(2) are shown in Fig. 3(e-g) and only the Mo and O elements are uniformly distributed. The sulphur elements disappeared in the white MO-S(2). These results demonstrate that sulphur was successfully doped during synthesis of MoO_{3-x}/S and disappeared during the heating process to form the final MoO_3 nanoflakes.

XRD and XPS patterns of the precursors α-MoO_3, the black intermediate MoO_{3-x}/S and the final products MoO_3 nanoflakes were analyzed to investigate the chemical composition of the samples and the valence and surface states of the elements. MO-S(2) was used as the representative. The diffraction peaks as shown by the black line in Fig. 4 indicate the high crystallinity orthorhombic structure of MO-S(2). The diffraction peaks for Au and Al_2O_3 are attributed to the ceramic substrate. As shown by the red line in Fig. 4, the XRD patterns of the black intermediate MoO_{3-x}/S confirmed its amorphous structure.

The XPS patterns of the precursors α-MoO_3, the intermediates MoO_{3-x}/S, and the MoO_3 nanoflakes are shown in Fig. 5(a). The black intermediate MoO_{3-x}/S is mainly composed of O, Mo and S, while the original α-MoO_3 and MoO_3 nanoflakes are mainly composed of O and Mo. This further demonstrated that sulphur was successfully doped during the synthesis of MoO_{3-x}/S and disappeared during the heating process, resulting in the formation of the final products MoO_3 nanoflakes. Fig. 5 (b-d) shows the Mo 3d doublet pattern of the precursors α-MoO_3, the black intermediate MoO_{3-x}/S, and the white final products MO-S(2), respectively. The peaks at 234.15 and 231 eV are corresponding for Mo $3d_{3/2}$ and Mo $3d_{5/2}$, respectively. The Mo 3d peaks in the black intermediate material can be deconvoluted into Mo^{6+} at 236.1 eV and 234 eV, Mo^{5+} at 232.8 eV, and Mo^{4+} at 231 eV and 229.8 eV. The Mo 3d peaks in the original α-MoO_3 and MO-S(2) can be deconvoluted into Mo^{6+} at 236.5 eV and 234.15 eV and Mo^{4+} at 231 eV [28,30,36]. The O 1 s peak in the XPS pattern of the precursors α-MoO_3 and MO-S(2) as shown in Fig. 5(e,f) was deconvoluted into adsorbed oxygen near 531 eV, surface oxygen near 529.7 eV, and lattice oxygen near 528.9 eV [30,36]. The proportions of surface oxygen species in precursors α-MoO_3 and MO-S(2) are 13.5% and 33.1%, respectively. This indicated that MO-S(2) improved the adsorption of oxygen species compared to the pristine α-MoO_3.

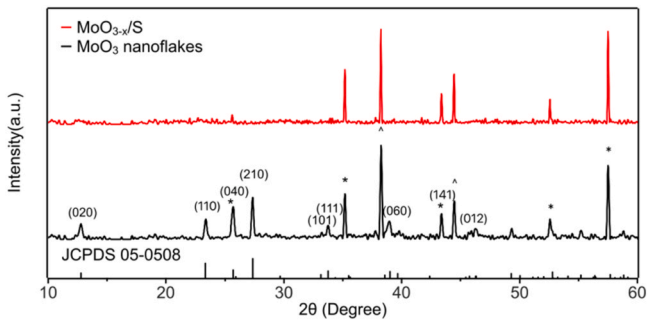

Fig. 4. The XRD spectra of MoO_3 nanoflakes of MO-S(2) and MoO_{3-x}/S. * and ^ peaks belong to Al_2O_3 and Au on the substrate, respectively.

3.2. Gas sensing performance

The impact of operating temperatures and nanostructures on the sensing performance of MoO_3-based gas sensors are shown in Fig. 6(a-e). Fig. 6(a) illustrates the response of MO, MO-S(0.5), MO-S(1), and MO-S (2) to 500 ppm ethanol at various operating temperatures. As the operating temperature increases, the response initially increases until it reaches a maximum at 350°C, after which it decreases. At the optimum operating temperature of 350°C, MO-S(0.5), MO-S(1), and MO-S(2) exhibit responses to 500 ppm of ethanol that are approximately 1.5, 2.1, and 3 times as high as MO does, respectively. MO, MO-S(0.5), MO-S (1), and MO-S(2) reached the maximum response at 350°C for 500 ppm acetone(Fig. 6(b)), methanol(Fig. 6(c)), and tert-butanol(Fig. 6(e)), and at 250°C for 500 ppm IPA(Fig. 6(d)). The response to various VOCs increased in the order of MO, MO-S(0.5), MO-S(1), and MO-S(2) as shown in Fig. 6(a-e). The R_a of MO, MO-S(0.5), MO-S(1), and MO-S(2) at various temperatures were recorded in Fig. S5. There is a decreasing trend on R_a of the four sensors as the operating temperature rises. The R_a of the sensors based on MoO_3 nanoflakes increased in the sequence of MO-S(0.5), MO-S(1), and MO-S(2). The difference in R_a among MoO_3 with different morphologies at the same operating temperature may be attributed to the reduced thickness and the looser stacking states of the nanoflakes. These will be discussed in the mechanism section.

MO-S(2) was exposed to ethanol gas of 1–1000 ppm at 350°C, respectively. Its dynamic response curve was depicted in Fig. 7(a). The relationship between the response and ethanol concentration (converted to logarithmic form) are linearly fitted as y=0.55049+0.48411x as shown in Fig. 7(b). The correlation coefficient R^2=0.99868 indicated the probability of using this sensor for ethanol concentration monitoring. In order to carry out the analysis for limit of detection (LOD) and limit of quantification (LOQ), the response to 1–1000 ppm ethanol was recorded as a function of concentration in Fig. S7(a). The LOD and LOQ were defined as $3S_a/b$ and $10S_a/b$, where S_a is the standard deviation of the response and b is the slope of the calibration curve [37,38]. Based on the linear extrapolation of the gas response as a function of ethanol concentration (Inset in Fig. S7(a)), the theoretical LOD and LOQ are 9.70 and 32.34 ppb, respectively. Fig. 7(c) shows the real-time resistance variation of MO-S(2) when exposed to 500 ppm ethanol at 350°C, the response time is 15 s and the recovery time is 150 s, respectively. The above performance characteristics of the sensor, including response intensity of 76.9 and response and recovery time of 15 s and 150 s, remain stable during five repeated measurement cycles as shown in Fig. 7(d). There was no trend of decay in response intensity of MO-S(2) to 500 ppm ethanol in two weeks as shown in Fig. 7(e). Between each mearsurement, the sensor was stored in ambient air. This two experimental results show that the gas sensor has good repeatability and long-term stability, which are also key parameters of gas sensors in practical applications.

Gas selectivity is a key parameter that reflects the ability of the gas sensor to identify the target gas. In this study, several VOCs, including acetone, methanol, IPA, and tert-butanol, which may interfere with the detection of ethanol, were measured for gas selectivity at different temperatures. Fig. 8(a,b) shows the comparison of the response of MO, MO-S(0.5), MO-S(1), and MO-S(2) to 500 ppm of ethanol, acetone, methanol, IPA, and tert-butanol at 200°C and 350°C, respectively. All the four gas sensors can selectively detect IPA at 200°C and ethanol at 350°C. The relationship between the response and IPA concentration (converted to logarithmic form) at 200°C was also fitted as shown in Fig. S6 to demonstrate the reliability of the sensor for IPA concentration monitoring. Fig. S7(b) shows the response to 1–1000 ppm IPA at 200°C as a function of concentration. The theoretical LOD and LOQ for IPA at 200°C are 15.29 and 50.95 ppb, respectively, derived from the linear extrapolation of the function (Inset in Fig. S7(b)). This result indicates that the sensor has a good detection capability for IPA and ethanol at 200°C and 350°C, respectively.

Moreover, the critical temperatures for the selectivity turned from

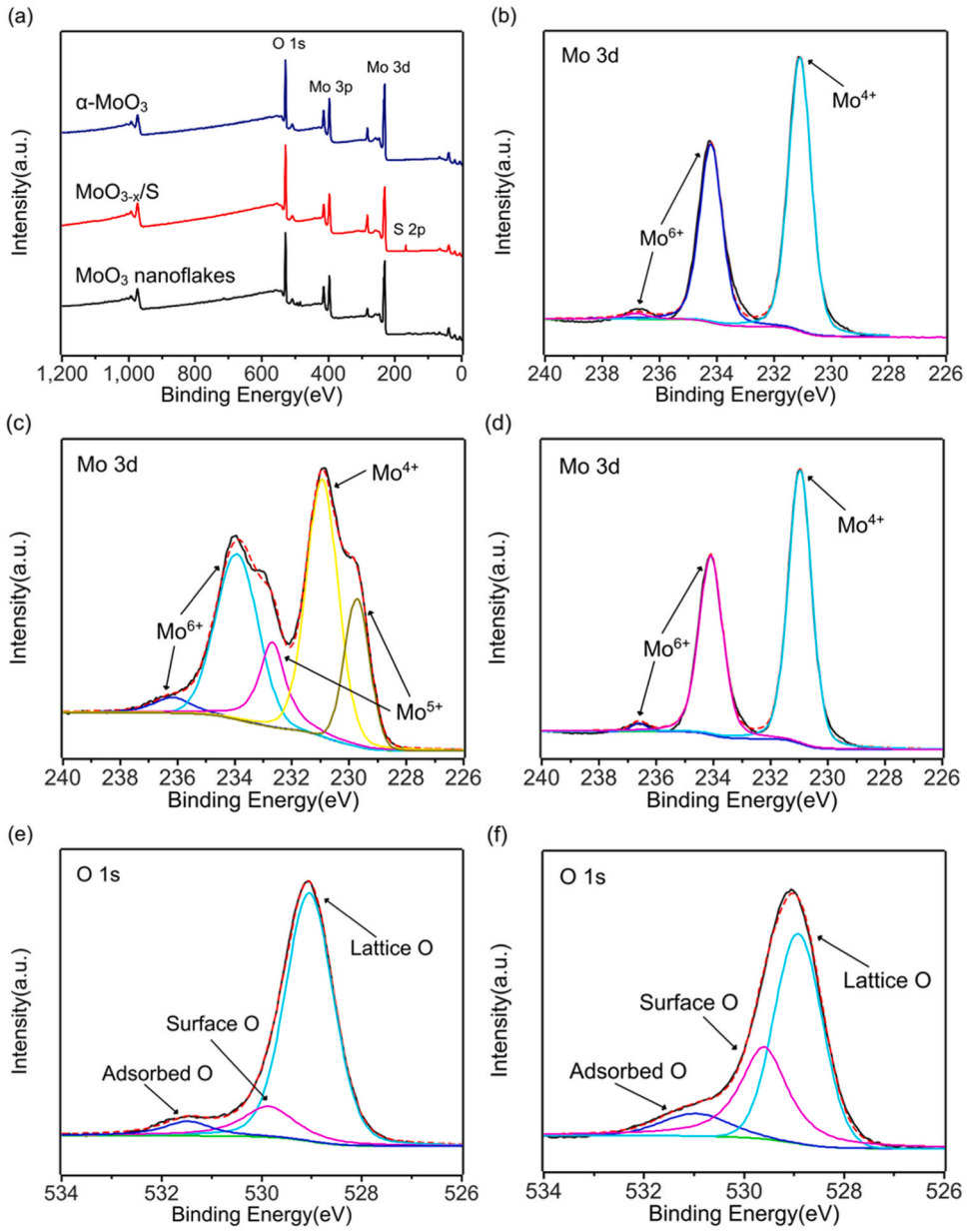

Fig. 5. XPS patterns of (a) survey spectra of the precursors α-MoO_3, intermediates MoO_{3-x}/S, and MoO_3 nanoflakes; (b)-(d) Mo 3d binding energy spectra of (b)α-MoO_3, (c)MoO_{3-x}/S and (d)MO-S(2); (e)-(f) O 1 s binding energy spectra of (e)α-MoO_3 and (f)MO-S(2).

IPA to ethanol are slightly different for the four typical devices. The ratio of the sensor response to ethanol and IPA was defined as the selectivity index, namely $K_{ethanol/IPA}$, to investigate the critical temperatures at which $K_{ethanol/IPA}$ located at 1. As shown in Fig. 8(c), $K_{ethanol/IPA}$ gradually increased with the operating temperature increasing and reached the maximum at 350°C. Furthermore, $K_{ethanol/IPA}$ is around 1 for all the four devices between 200°C and 250°C, indicating that the critical temperatures for all of the four devices are in this temperature range. We therefore carried out more detailed sensing measurements between 200°C and 250°C. As shown in the inset of Fig. 8(c), the critical temperatures of MO, MO-S(0.5), MO-S(1), and MO-S(2) are at 240°C, 235°C, 220°C, and 210°C, respectively, showing a decreasing trend.

A comparison of the sensing properties of the MoO_3-based ethanol sensors was conducted between our MO-S(2) and results reported in literatures. As shown in Table 1, the sensing performance for ethanol of the MoO_3 nanoflakes in this study is superior to the reported results slightly, reflected by higher response or shorter response time.

3.3. Sensing mechanism

The gas sensing mechanism of MOS based gas sensors is usually related to the surface adsorption and reactions [13,44–46]. Fig. 9 depicts the ethanol sensing mechanism diagrams of MoO_3 nanoflakes. When the sensitive material MoO_3 is placed in clean air, oxygen molecules will be chemisorbed on the surface of MoO_3 by capturing electrons in the conduction band of MoO_3 to form chemisorbed oxygen species (O_2^-, T < 100°C; O^-, 100 < T < 300°C; O^{2-}, T > 300°C) [47,48], which leads to the formation of electron depletion layer and the reduction of carrier concentration [49–52]. The reactions that took place are given in Eqs. (1)-(3):

$$O_{2\,(gas)} + 2e^- \rightarrow O_{2\,(ads)}^- \quad (1)$$

$$O_{2\,(gas)} + e^- \rightarrow O_{(ads)}^- \quad (2)$$

$$O_{2\,(gas)} + 2e^- \rightarrow O_{(ads)}^{2-} \quad (3)$$

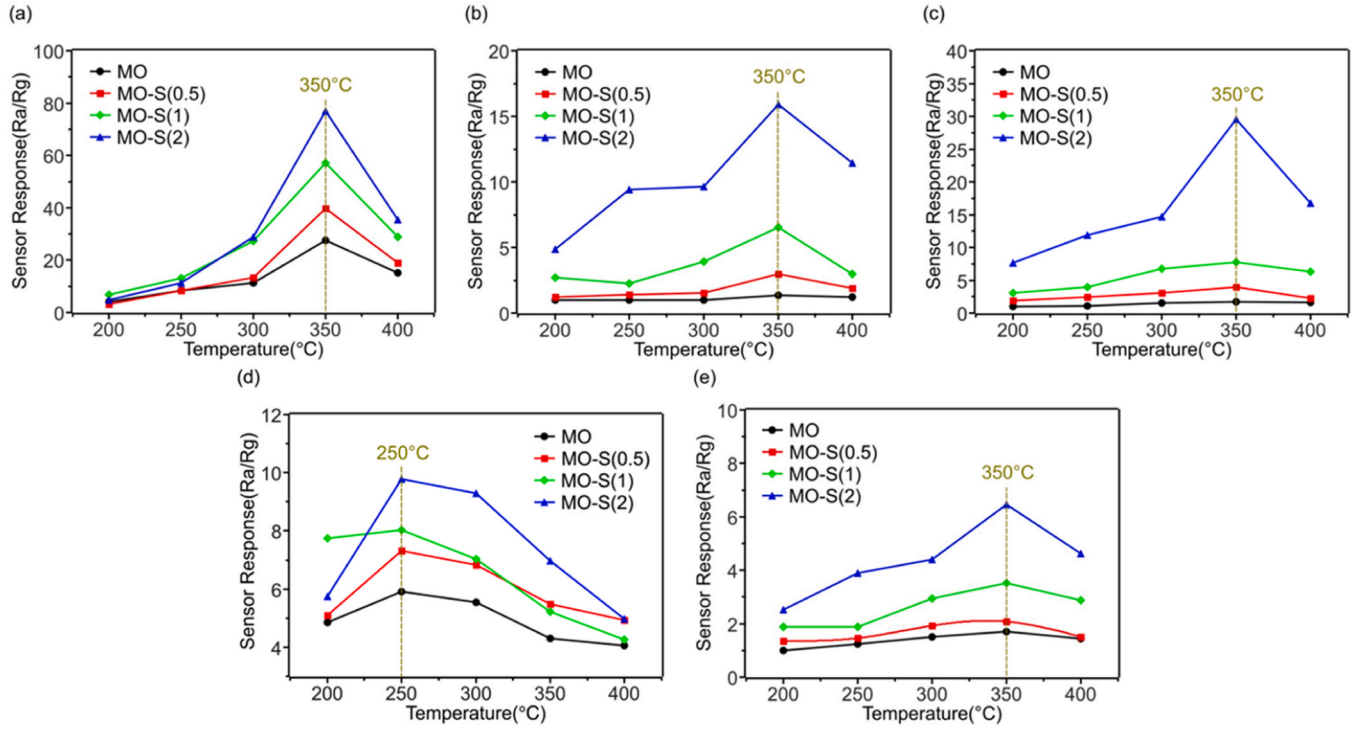

Fig. 6. Response versus working temperature of MO, MO-S(0.5), MO-S(1), and MO-S(2) to (a) 500 ppm ethanol; (b) 500 ppm acetone; (c) 500 ppm methanol; (d) 500 ppm IPA; (e) 500 ppm tert-butanol.

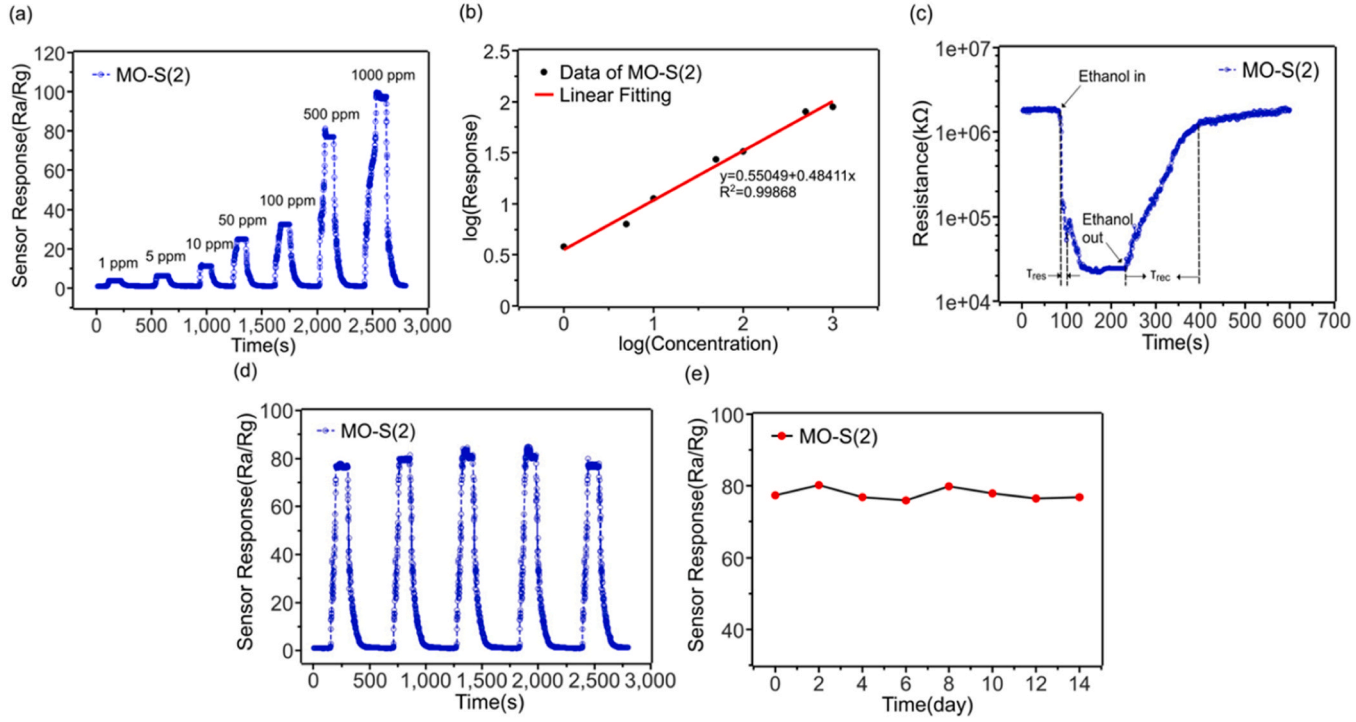

Fig. 7. (a) Dynamic response curves of MO-S(2) to 1–1000 ppm ethanol, and (b) corresponding fitting curves; (c) Response/recovery times, (d) Repeatability and (e) stability of MO-S(2) towards 500 ppm ethanol at 350°C.

When MoO_3 is exposed to the reducing gas, such as ethanol, acetone, methanol, IPA, tert-butanol studied herein, the gas molecules react with the chemically adsorbed oxygen ions, and the electrons are released back to MoO_3, leading to a decrease in the width of the electron depletion layer and an increase in the concentration of electron carriers.

The above process is described by Eqs. (4)-(8):

$$C_2H_5OH_{(gas)} + 6O^{n-}_{(ads)} \rightarrow 3H_2O + 2CO_2 + 6ne^- \quad (4)$$

$$CH_3COCH_{3(gas)} + 8O^{n-}_{(ads)} \rightarrow 3CO_2 + 3H_2O + 8ne^- \quad (5)$$

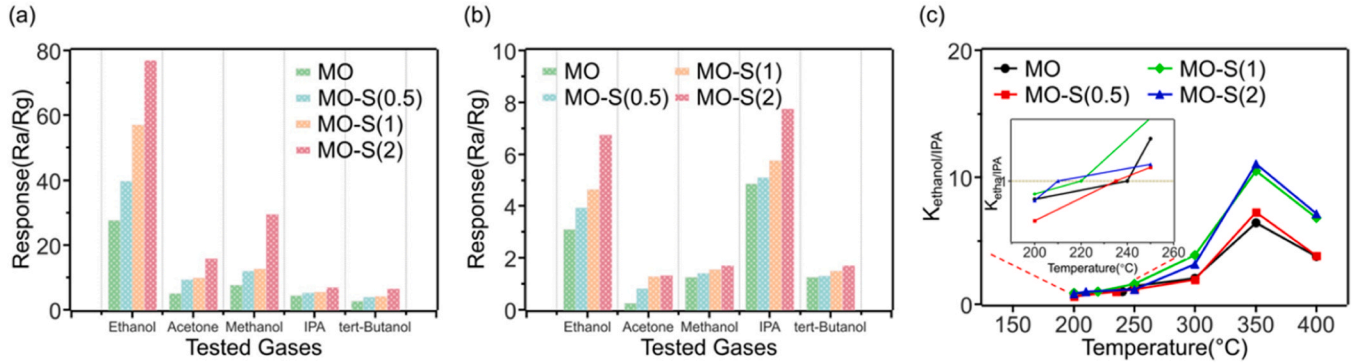

Fig. 8. Selectivity histogram of MO, MO-S(0.5), MO-S(1), MO-S(2) at (a) 350°C and (b) 200°C; (c) Selective index between ethanol and IPA versus working temperature of MO, MO-S(0.5), MO-S(1), MO-S(2). The inset represents the critical temperatures where the selective index is around 1, indicating that the selectivity turned from IPA to ethanol.

Table 1
Summary of the sensing properties of MoO_3-based ethanol sensors in previous literatures and in this work.

Sensing meterials	Ethanol concentration (ppm)	Temperature (°C)	Response (R_a/R_g)	τ_{res}(s)	Refs.
MoO_3 nanosheets	100	300	32.4	21	[23]
MoO_3 thin films	500	300	38	<75	[39]
Crystalline/ Amorphous Core/Shell MoO_3 composites	500	180	56	/	[40]
MoO_3 nanoplates	100	400	13	7	[41]
MoO_3 microrods	500	332	8.5	/	[42]
MoO_3 nanorods	100	250	19.8	15	[43]
MoO_3 nanoflakes	100/500	350	32.4/76.9	15	this work

$$CH_3OH_{(gas)} + 3O^{n-}_{(ads)} \rightarrow 2H_2O + CO_2 + 3ne^- \quad (6)$$

$$C_3H_7OH_{(gas)} + 9O^{n-}_{(ads)} \rightarrow 2H_2O + CO_2 + 9ne^- \quad (7)$$

$$C_4H_9OH_{(gas)} + 12O^{n-}_{(ads)} \rightarrow 2H_2O + CO_2 + 12ne^- \quad (8)$$

The thickness of materials plays a critical role in conduction mechanism, which is probably related to the Debye length of semiconductors [53]. The Debye length of a material is known as the length of the space charge layer or surface electron depletion layer, which can be derived according to the following Eq. (9):

$$\lambda_D = \sqrt{\frac{\varepsilon_0 \varepsilon K_B T}{q^2 n_c}} \quad (9)$$

Where ε_0 is the permittivity of free space, ε the dielectric constant of the materials, K_B the Boltzmann constant, T the temperature, q the charge of electron and n_c the concentration of electron [54]. The Debye length of MoO_3 is 2.2 nm at 350°C.

In this study, the increase of S-doping in the preparation process caused the MoO_3 to become thinner, longer and narrower, resulting in the nanostructures changing from nanoflakes to the one-dimensional nanoribbons. The increased aspect ratio and decreased thickness are both beneficial for gas sensing applications. As the thickness of the nanoflakes decreases, the electron depletion layers formed in air due to oxygen adsorption occupy a greater proportion of the material and cause the increase in R_a [55]. The decreased thickness of MoO_3 nanoflakes means that it approaches twice the Debye length so that the change in resistance caused by gas sensing will transform from a change in surface resistance to a more sufficient change in body resistance, thus providing a higher response. It is consistent with the decreased thickness in their morphology that the R_a and response of the sensors based on MoO_3 nanoflakes increased in the order of MO-S(0.5), MO-S(1), and MO-S(2). Besides, the stacked state of MoO_3, which changes from compact to loose as shown in Fig. 3(b-d), will increase the R_a as well as enhance the gas diffusion and increase the contact area between the surface of the sensor and the gas molecules. The reactive species also affect the interaction between the sensitive material and the gas. There are three types of

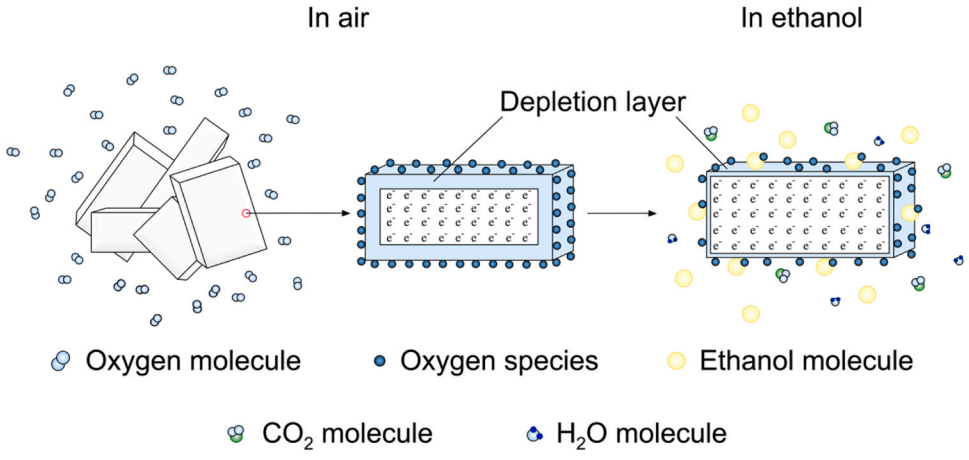

Fig. 9. Gas sensing mechanism diagrams of MoO_3 nanoflakes exposed to air and ethanol, respectively.

oxygen species on MoO_3 when it is exposed to air: adsorbed oxygen (physical adsorption), surface oxygen (chemisorption), and lattice oxygen (crystal formation) [30,56]. Among them, surface oxygen undergoes a redox reaction with the target gas to be measured during the gas sensing process. The O 1 s peak in the XPS patterns of MO-S(2), MO-S(1), MO-S(0.5), MO was deconvoluted into three peaks corresponding to the above three oxygen species as shown in Fig. 10. The proportions of surface oxygen species in MO, MO-S(0.5), MO-S(1), MO-S(2) are 13.5%, 19.0%, 29.3%, 33.1%, respectively. The proportion of surface oxygen species in the MoO_3 obtained increases by increasing the S-doping in the preparation process. This increases the surface oxygen species available for the redox reaction required for gas sensing, contributing to the improved response to the five measured gases.

According to the sensing mechanism mentioned above, stronger adsorption between the gas and the material, and faster redox reaction will contribute to the gas selectivity. Herein, MoO_3 nanoflakes exhibit selectivity to IPA at 200°C and ethanol at 350°C, respectively. When the working temperature of the sensor is relatively lower, the interaction between the MoO_3 and the gas is mainly affected by the electron releasing nature (+I effect) of the functional groups in the VOCs molecules [57]. Alcohol molecules are classified into 1° alcohol, 2° alcohol, and 3° alcohol based on the number of carbon atoms attached to the hydroxyl group. Ethanol and IPA are 1° alcohol and 2° alcohol [58] because the hydroxyl group is respectively attached to the first and second carbon atom on the carbon chain, respectively. In an ethanol molecule(1° alcohol), the hydroxyl group is directly connected to the carbon atom and a C-OH bond is formed. Since the oxygen atom is more electronegative than the carbon atom, the electrons in the C-OH bond will be attracted by the oxygen atom, which reduces the electron density of the hydroxyl group, thereby weakening its ability to lose electrons. However, in an IPA (2° alcohol) molecule, the hydroxyl group is connected to the second carbon atom. This is equivalent to replacing a hydrogen atom in the carbon chain of the ethanol molecule with a methyl group (-CH_3). The methyl group acts as an electron donor, providing a higher electron density to neighbouring hydroxyl groups and, making it easier to donate electrons and having stronger electron releasing properties. Compared with ethanol, the oxygen demand in the IPA reaction is lower due to its higher electron donating properties. This might contribute to the result that the selectivity temperature for IPA is relatively lower than for ethanol [58]. When the working temperature increases, the interaction between the sensitive material and the gas molecules becomes more complete. Due to its stronger reducing property, ethanol has a stronger interaction with reactive oxygen species on the surface of MoO_3, while the chemical properties of IPA are relatively stable [23]. As a result, MoO_3 nanoflakes exhibit relative selectivity for ethanol at 350°C.

4. Conclusion

In summary, we reported a strategy for the synthesis of MoO_3 nanoflakes, using S-doping to modify their aspect ratio and thickness. With increasing the amount of the doped S in the preparation process, the thickness of MoO_3 nanoflakes decreased remarkably, the aspect ratio increased and the surface chemisorbed oxygen increased. The nanostructure of the obtained MoO_3 changed from nanoflakes to one-dimensional nanoribbons. These all contributed to the improved gas sensing performance. MO-S(2) had a response of 76.9–500 ppm ethanol, which was about 3 times that of MO. A temperature-dependent dual selectivity to IPA and ethanol was reported. The critical temperatures are 240°C, 235°C, 220°C, and 210°C for MO, MO-S(0.5), MO-S(1), and MO-S(2), respectively. These results demonstrate that increasing S-doping in the preparation process of MoO_3 will not only increase the response magnitude but also decrease the critical temperatures for the dual selectivity. Finally, based on the sensing mechanism, the improved sensing performance of MoO_3 nanoflakes with temperature-dependent dual selectivity were attributed to the decreased thickness, increased aspect ratio, increased chemisorbed oxygen, etc. The feasibility of inducing S-doping in the preparation methods to modify the

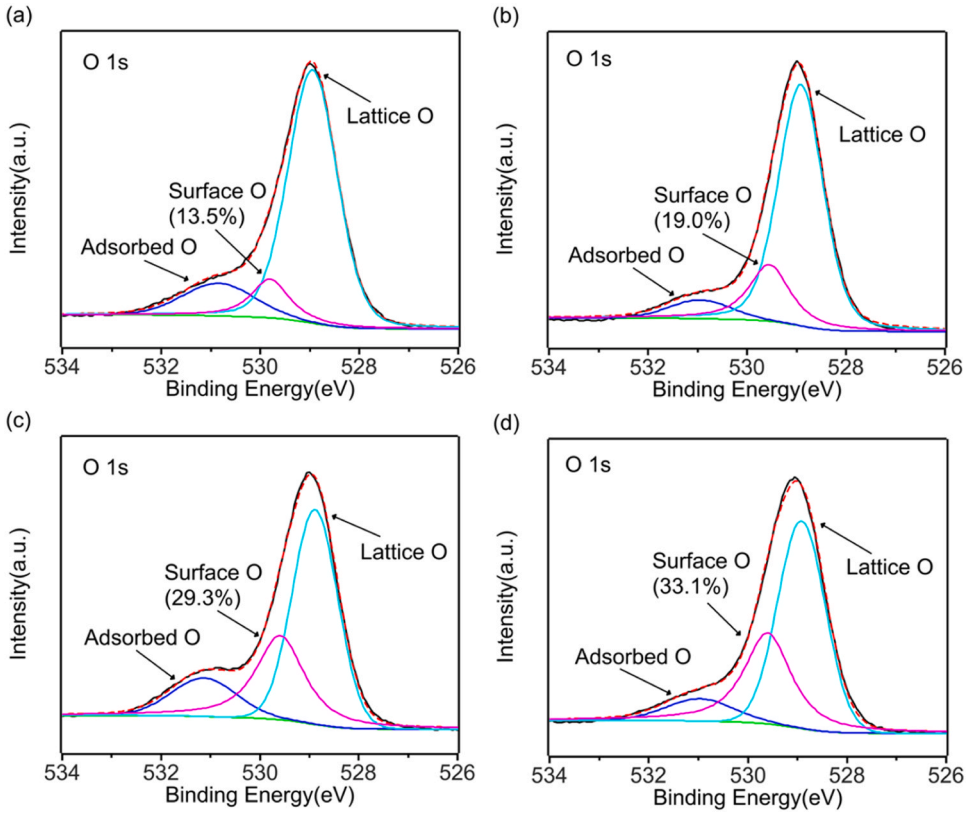

Fig. 10. O 1 s binding energy spectra of (a) MO, (b) MO-S(0.5), (c) MO-S(1), and (d) MO-S(2).

nanostructures of MoO_3 nanoflakes and using it to enhance the gas sensing performance are reported for the first time. This should have the potential to be widely adopted in applications where higher aspect ratio is beneficial, such as various sensors and photocatalysis.

CRediT authorship contribution statement

Aiwu Wang: Funding acquisition, Methodology. **Wen Li:** Conceptualization, Data curation, Formal analysis, Investigation, Methodology, Validation, Writing – original draft, Writing – review & editing. **Hao Xu:** Methodology, Writing – original draft. **Fang Xu:** Conceptualization, Funding acquisition, Methodology, Project administration, Resources, Supervision, Writing – review & editing. **Liaoyuan Zhang:** Writing – review & editing. **Zhiyong Fan:** Writing – review & editing. **Aihua Zhong:** Funding acquisition, Methodology. **Yujie Ma:** Funding acquisition. **Xuelan Cheng:** Writing – review & editing. **Jidong Shi:** Formal analysis, Supervision.

Declaration of Competing Interest

The authors declare that they have no known competing financial interests or personal relationships that could have appeared to influence the work reported in this paper.

Data availability

No data was used for the research described in the article.

Acknowledgements

This study was supported by National Natural Science Foundation of China [Grant Numbers: 62001308, 22109104, 20211062020033], Shenzhen Science and Technology Program [Grant Number: RCBS20210609103736094], Natural Science Foundation of Top Talent of SZTU [Grant Numbers: 20200219 and GDRC202101], Youth Innovation Talent Project of Guangdong Education Department [Grant Number: 2021KQNCX081].

Appendix A. Supporting information

Supplementary data associated with this article can be found in the online version at doi:10.1016/j.snb.2024.135548.

References

[1] Q. Zhou, et al., Diverse scenarios selective perception of H_2S via cobalt sensitized MOF filter membrane coated three-dimensional metal oxide sensor, Chem. Eng. J. vol. 450 (2022) 138014, https://doi.org/10.1016/j.cej.2022.138014.
[2] E. Gonzalez, E. Llobet, A. Romero, X. Vilanova, A new approach to NO_2 gas sensing based on pulsed UV Light and FFT analysis using MOX sensors, IEEE Sens. J. vol. 20 (1) (2020) 397–404, https://doi.org/10.1109/JSEN.2019.2942490.
[3] S. Zhang, et al., An acetone gas sensor based on nanosized Pt-loaded Fe_2O_3 nanocubes, Sens. Actuators B Chem. vol. 290 (2019) 59–67, https://doi.org/10.1016/j.snb.2019.03.082.
[4] H. Du, et al., Highly selective acetone detector based on a separation channel and semiconductor gas sensor, Meas. Sci. Technol. vol. 32 (8) (2021) 085102, https://doi.org/10.1088/1361-6501/abe666.
[5] L. Li, et al., Hollow-out Fe_2O_3 -loaded NiO heterojunction nanorods enable real-time exhaled ethanol monitoring under high humidity, ACS Appl. Mater. Interfaces vol. 15 (12) (2023) 15707–15720, https://doi.org/10.1021/acsami.2c23088.
[6] Y. Zhao, et al., Selective detection of methane by Pd-In_2O_3 sensors with a catalyst filter film, Sens. Actuators B Chem. vol. 328 (2021) 129030, https://doi.org/10.1016/j.snb.2020.129030.
[7] Y. Yong, et al., Highly sensitive and selective gas sensors based on nanoporous CN monolayer for reusable detection of NO, H_2S and NH_3: a first-principles study, Appl. Surf. Sci. vol. 606 (2022) 154806, https://doi.org/10.1016/j.apsusc.2022.154806.
[8] Y. Wang, Y. Cui, X. Meng, Z. Zhang, J. Cao, A gas sensor based on Ag-modified ZnO flower-like microspheres: temperature-modulated dual selectivity to CO and CH_4, Surf. Interfaces vol. 24 (2021) 101110, https://doi.org/10.1016/j.surfin.2021.101110.
[9] T. Seiyama, A. Kato, K. Fujiishi, M. Nagatani, A new detector for gaseous components using semiconductive thin films, Anal. Chem. vol. 34 (11) (1962) 1502–1503, https://doi.org/10.1021/ac60191a001.
[10] P. Li, et al., Cr-doped NiO nanoparticles as selective and stable gas sensor for ppb-level detection of benzyl mercaptan, Sens. Actuators B Chem. vol. 339 (2021) 129886, https://doi.org/10.1016/j.snb.2021.129886.
[11] Z. Lu, C. Lou, A. Cheng, J. Zhang, J. Sun, A sensitive and ultrafast $FA_{0.83}Cs_{0.17}PbI_3$ perovskite sensor for NO_2 detection at room temperature, J. Alloy. Compd. vol. 919 (2022) 165831, https://doi.org/10.1016/j.jallcom.2022.165831.
[12] S. Jeong, et al., A new strategy for detecting plant hormone ethylene using oxide semiconductor chemiresistors: exceptional gas selectivity and response tailored by nanoscale Cr_2O_3 catalytic overlayer, Adv. Sci. vol. 7 (7) (2020) 1903093, https://doi.org/10.1002/advs.201903093.
[13] M. Ghazi, S. Janfaza, H. Tahmooressi, N. Tasnim, M. Hoorfar, Selective detection of VOCs using microfluidic gas sensor with embedded cylindrical microfeatures coated with graphene oxide, J. Hazard. Mater. vol. 424 (2022) 127566, https://doi.org/10.1016/j.jhazmat.2021.127566.
[14] J. Wang, S. Fan, Y. Xia, C. Yang, S. Komarneni, Room-temperature gas sensors based on ZnO nanorod/Au hybrids: visible-light-modulated dual selectivity to NO_2 and NH_3, J. Hazard. Mater. vol. 381 (2020) 120919, https://doi.org/10.1016/j.jhazmat.2019.120919.
[15] J. Li, et al., Construction of SnO_2 nanoneural network by ultrasmall particles for highly selective NO_2 detection at low temperature, Sens. Actuators B Chem. vol. 361 (2022) 131703, https://doi.org/10.1016/j.snb.2022.131703.
[16] H. Yang, et al., A simple gas sensor based on zinc ferrite hollow spheres: highly sensitivity, excellent selectivity and long-term stability, Sens. Actuators B Chem. vol. 280 (2019) 34–40, https://doi.org/10.1016/j.snb.2018.10.056.
[17] T.T.N. Hoa, et al., Highly selective H_2S gas sensor based on WO_3-coated SnO_2 nanowires, Mater. Today Commun. vol. 26 (2021) 102094, https://doi.org/10.1016/j.mtcomm.2021.102094.
[18] J.-F. Tang, C.-C. Fang, C.-L. Hsu, Enhanced organic gas sensor based on Cerium- and Au-doped ZnO nanowires via low temperature one-pot synthesis, Appl. Surf. Sci. vol. 613 (2023) 156094, https://doi.org/10.1016/j.apsusc.2022.156094.
[19] A. Umar, et al., CdO–ZnO nanorices for enhanced and selective formaldehyde gas sensing applications, Environ. Res. vol. 200 (2021) 111377, https://doi.org/10.1016/j.envres.2021.111377.
[20] F. Xu, H.-F. Lv, S.-Y. Wu, H.-P. Ho, Light-activated gas sensing activity of ZnO nanotetrapods enhanced by plasmonic resonant energy from Au nanoparticles, Sens. Actuators B Chem. vol. 259 (2018) 709–716, https://doi.org/10.1016/j.snb.2017.12.128.
[21] H.M.M. Munasinghe Arachchige, D. Zappa, N. Poli, N. Gunawardhana, E. Comini, Gold functionalized MoO_3 nano flakes for gas sensing applications, Sens. Actuators B Chem. vol. 269 (2018) 331–339, https://doi.org/10.1016/j.snb.2018.04.124.
[22] R. Malik, N. Joshi, V.K. Tomer, Advances in the designs and mechanisms of MoO_3 nanostructures for gas sensors: a holistic review, Mater. Adv. vol. 2 (13) (2021) 4190–4227, https://doi.org/10.1039/D1MA00374G.
[23] F. Ji, et al., 2D-MoO_3 nanosheets for superior gas sensors, Nanoscale vol. 8 (16) (2016) 8696–8703, https://doi.org/10.1039/C6NR00880A.
[24] T. Liu, B. Li, Y. Hao, Z. Yao, MoO_3-nanowire membrane and $Bi_2Mo_3O_{12}/MoO_3$ nano-heterostructural photocatalyst for wastewater treatment, Chem. Eng. J. vol. 244 (2014) 382–390, https://doi.org/10.1016/j.cej.2014.01.070.
[25] Md Maniruzzaman, M. Arifur Rahman, K. Jeong, J. Lee, MoO_3/Au/MoO_3–PEDOT:PSS multilayer electrodes for ITO-free organic solar cells, Mater. Sci. Semicond. Process. vol. 27 (2014) 114–120, https://doi.org/10.1016/j.mssp.2014.06.034.
[26] J.-Y. Park, H.-K. Kim, Flexible metal/oxide/metal transparent electrodes made of thermally evaporated MoO_3 /Ag/MoO_3 for thin film heaters, Phys. Status Solidi A vol. 215 (23) (2018) 1800674, https://doi.org/10.1002/pssa.201800674.
[27] S.-K. Shen, et al., Sensing mechanism of Ag/α-MoO_3 nanobelts for H_2S gas sensor, Rare Met vol. 40 (6) (2021) 1545–1553, https://doi.org/10.1007/s12598-020-01647-3.
[28] F. Rahman, et al., Dual selective gas sensing characteristics of 2D α-MoO_{3-x} via a facile transfer process, ACS Appl. Mater. Interfaces vol. 11 (43) (2019) 40189–40195, https://doi.org/10.1021/acsami.9b11311.
[29] X. Luo, et al., Rapid hydrogen sensing response and aging of α-MoO_3 nanowires paper sensor, Int. J. Hydrog. Energy vol. 42 (12) (2017) 8399–8405, https://doi.org/10.1016/j.ijhydene.2017.01.116.
[30] Z. Tang, et al., MoO_3 nanoflakes coupled reduced graphene oxide with enhanced ethanol sensing performance and mechanism, Sens. Actuators B Chem. vol. 297 (2019) 126730, https://doi.org/10.1016/j.snb.2019.126730.
[31] F. Xu, et al., Expanding selectivity functionality of a ZnO nanotetrapod-based volatile organic compound sensor using Au nanoparticle decoration, ACS Appl. Nano Mater. vol. 6 (10) (2023) 8335–8345, https://doi.org/10.1021/acsanm.3c00576.
[32] P. Barik, M. Pradhan, Selectivity in trace gas sensing: recent developments, challenges, and future perspectives, Analyst vol. 147 (6) (2022) 1024–1054, https://doi.org/10.1039/D1AN02070F.
[33] M. Tonezzer, T.T.L. Dang, Q.H. Tran, S. Iannotta, Dual-selective hydrogen and ethanol sensor for steam reforming systems, Sens. Actuators B Chem. vol. 236 (2016) 1011–1019, https://doi.org/10.1016/j.snb.2016.04.150.
[34] F. Xu, C. Zhou, H.-P. Ho, A rule for operation temperature selection of a conductometric VOC gas sensor based on ZnO nanotetrapods, J. Alloy. Compd. vol. 858 (2021) 158294, https://doi.org/10.1016/j.jallcom.2020.158294.
[35] K. Chan, The response of the Intox EC/IR II to isopropanol and isopropanol/ethanol mixtures, Can. Soc. Forensic Sci. J. vol. 51 (3–4) (2018) 67–82, https://doi.org/10.1080/00085030.2018.1491691.

[36] M.M. Mohamed, T.M. Salama, M. Morsy, R.M.A. Shahba, S.H. Mohamed, Facile strategy of synthesizing α-MoO_{3-x} nanorods boosted as traced by 1% graphene oxide: Efficient visible light photocatalysis and gas sensing applications, Sens. Actuators B Chem. vol. 299 (2019) 126960, https://doi.org/10.1016/j.snb.2019.126960.
[37] A. Shrivastava, V. Gupta, Methods for the determination of limit of detection and limit of quantitation of the analytical methods, Chron. Young Sci. vol. 2 (1) (2011) 21, https://doi.org/10.4103/2229-5186.79345.
[38] C. Su, et al., Controllable synthesis of heterostructured CuO–NiO nanotubes and their synergistic effect for glycol gas sensing, Sens. Actuators B Chem. vol. 304 (Feb. 2020) 127347, https://doi.org/10.1016/j.snb.2019.127347.
[39] N. Illyaskutty, H. Kohler, T. Trautmann, M. Schwotzer, V.P.M. Pillai, Enhanced ethanol sensing response from nanostructured MoO_3:ZnO thin films and their mechanism of sensing, J. Mater. Chem. C. vol. 1 (25) (2013) 3976, https://doi.org/10.1039/c3tc30408f.
[40] L. Wang, et al., Synthesis of crystalline/amorphous core/shell MoO_3 composites through a controlled dehydration route and their enhanced ethanol sensing properties, Cryst. Growth Des. vol. 14 (2) (2014) 569–575, https://doi.org/10.1021/cg401384t.
[41] D. Chen, et al., Single-crystalline MoO_3 nanoplates: topochemical synthesis and enhanced ethanol-sensing performance, J. Mater. Chem. vol. 21 (25) (2011) 9332, https://doi.org/10.1039/c1jm11447f.
[42] Y. Liu, S. Yang, Y. Lu, N.V. Podval'naya, W. Chen, G.S. Zakharova, Hydrothermal synthesis of h-MoO_3 microrods and their gas sensing properties to ethanol, Appl. Surf. Sci. vol. 359 (2015) 114–119, https://doi.org/10.1016/j.apsusc.2015.10.071.
[43] Y. Xia, C. Wu, N. Zhao, H. Zhang, Spongy MoO_3 hierarchical nanostructures for excellent performance ethanol sensor, Mater. Lett. vol. 171 (2016) 117–120, https://doi.org/10.1016/j.matlet.2015.12.159.
[44] F. Yan, et al., Low operating temperature and highly selective NH_3 chemiresistive gas sensors based on Ag_3PO_4 semiconductor, Appl. Surf. Sci. vol. 479 (2019) 1141–1147, https://doi.org/10.1016/j.apsusc.2019.02.184.
[45] S. Hou, et al., Synergistic CNFs/CoS_2 /MoS_2 flexible films with unprecedented selectivity for NO gas at room temperature, p. acsami.0c05953, ACS Appl. Mater. Interfaces (2020), https://doi.org/10.1021/acsami.0c05953.
[46] S. Yang, et al., Au@ZnO functionalized three–dimensional macroporous WO_3: a application of selective H_2S gas sensor for exhaled breath biomarker detection, Sens. Actuators B Chem. vol. 324 (2020) 128725, https://doi.org/10.1016/j.snb.2020.128725.
[47] H. Ji, W. Zeng, Y. Li, Gas sensing mechanisms of metal oxide semiconductors: a focus review, Nanoscale vol. 11 (47) (2019) 22664–22684, https://doi.org/10.1039/C9NR07699A.
[48] D.Pravarthana Nagmani, A. Tyagi, T.C. Jagadale, W. Prellier, D.K. Aswal, Highly sensitive and selective H_2S gas sensor based on TiO_2 thin films, Appl. Surf. Sci. vol. 549 (2021) 149281, https://doi.org/10.1016/j.apsusc.2021.149281.
[49] B. Karunagaran, P. Uthirakumar, S.J. Chung, S. Velumani, E.-K. Suh, TiO_2 thin film gas sensor for monitoring ammonia, Mater. Charact. vol. 58 (8–9) (2007) 680–684, https://doi.org/10.1016/j.matchar.2006.11.007.
[50] N.S. Ramgir, et al., Growth and gas sensing characteristics of p- and n-type ZnO nanostructures, Sens. Actuators B Chem. vol. 156 (2) (2011) 875–880, https://doi.org/10.1016/j.snb.2011.02.058.
[51] M.M. Arafat, B. Dinan, S.A. Akbar, A.S.M.A. Haseeb, Gas sensors based on one dimensional nanostructured metal-oxides: a review, Sensors vol. 12 (6) (2012) 7207–7258, https://doi.org/10.3390/s120607207.
[52] Z. Yang, L.-M. Li, Q. Wan, Q.-H. Liu, T.-H. Wang, High-performance ethanol sensing based on an aligned assembly of ZnO nanorods, Sens. Actuators B Chem. vol. 135 (1) (2008) 57–60, https://doi.org/10.1016/j.snb.2008.07.016.
[53] J. Wang, S. Fan, Y. Xia, C. Yang, S. Komarneni, Room-temperature gas sensors based on ZnO nanorod/Au hybrids: visible-light-modulated dual selectivity to NO_2 and NH_3, J. Hazard. Mater. vol. 381 (2020) 120919, https://doi.org/10.1016/j.jhazmat.2019.120919.
[54] Y. Xu, L. Zheng, C. Yang, W. Zheng, X. Liu, J. Zhang, Chemiresistive sensors based on core-shell ZnO@TiO_2 nanorods designed by atomic layer deposition for n-butanol detection, Sens. Actuators B Chem. vol. 310 (2020) 127846, https://doi.org/10.1016/j.snb.2020.127846.
[55] Y. Hu, O.K. Tan, J.S. Pan, H. Huang, W. Cao, The effects of annealing temperature on the sensing properties of low temperature nano-sized $SrTiO_3$ oxygen gas sensor, Sens. Actuators B Chem. vol. 108 (1–2) (2005) 244–249, https://doi.org/10.1016/j.snb.2004.10.053.
[56] J. Guo, H. Li, Q. Ma, Q. Zhang, Y. Wang, X. Wang, Surface oxygen vacancies actuated MoO_3/$CuMoO_4$ self-assembled microspheres for highly selective triethylamine detection, Sens. Actuators B Chem. vol. 369 (2022) 132256, https://doi.org/10.1016/j.snb.2022.132256.
[57] M.G. Voronkov, E.I. Brodskaya, V.V. Belyaeva, and N.F. Lazareva, "The nature of the super-electron-releasing inductive effect of the silatranyl group and its spectroscopic and chemical consequences," vol. 50, no. 5, 2001.
[58] S. Dey, S. Santra, S.K. Ray, P.K. Guha, $Fe_x Ni_{(1-x)}$ O/NiO Heterojunction-Based Selective VOC Sensor Device by Using Temperature Tunability, IEEE Sens. J. vol. 20 (14) (2020) 7503–7508, https://doi.org/10.1109/JSEN.2019.2962182.

Wen Li is currently working on her master's degree in Shenzhen Technology University. Her main research interest is in semiconductor-based gas sensors, focusing on gas selectivity.

Hao Xu received his master degree from Shihezi University, China. His research focused on the nanofabrication and chemical sensors.

Aiwu Wang received the Ph.D. degree from City University of Hong Kong in 2018. Currently, he is an assistant professor in Shenzhen Technology University. His main research areas are low-dimensional carbon nanostructures for LEDs, sensors, catalysis, and bioimaging.

Xuelan Cheng currently works on her master's degree in Shenzhen Technology University. Her main research interest is in semiconductor-based gas sensors, focusing on room-temperature gas sensing.

Jidong Shi received the Ph.D. degree from National Center for Nanoscience, Chinese Academy of Sciences (NCNS). Currently, he is an assistant professor in Shenzhen Technology University. His research interests include wearable flexible sensors and piezoelectric catalytic systems.

Aihua Zhong received the Ph.D. degree from Tohoku University in 2014. Currently, he is an assistant professor in Shenzhen University. He is mainly engaged in the research of gas/photoelectric sensor arrays, electronic noses, thermoelectric thin films and micro-nano devices.

Yujie Ma received the Ph.D. degree from Shandong University in 2014. Currently, she is an assistant professor in Shenzhen Technology University. Her main research interests include integrated optoelectronic devices, preparation of optical single-crystal thin-film heterostructures, ion-radiation effects and material modification studies.

Liaoyuan Zhang currently works on the master's degree in Shenzhen Technology University. His research interest is in optoelectronic devices.

Zhiyong Fan received Ph.D. degree from University of California, Irvine in 2006. Currently, he is a chair professor in Hong Kong University of Science and Technology. His main research interests include smart gas sensors, electronic-nose, nanoelectronic design, nanofabrication, and nanomaterials.

Fang Xu received the Ph.D. degree from Chinese University of Hong Kong in 2018. Currently, she is an assistant professor in Shenzhen Technology University. Her main research interests include semiconductor-based gas sensors, nanomaterials and optoelectronic devices.